OPTICS

Engineering phonon polaritons in van der Waals heterostructures to enhance in-plane optical anisotropy

Kundan Chaudhary[1]*, Michele Tamagnone[1]*†, Mehdi Rezaee[1,2]*, D. Kwabena Bediako[3], Antonio Ambrosio[4], Philip Kim[3], Federico Capasso[1]†

Van der Waals (vdW) heterostructures assembled from layers of two-dimensional materials have attracted considerable interest due to their novel optical and electrical properties. Here, we report a scattering-type scanning near-field optical microscopy study of hexagonal boron nitride on black phosphorus (h-BN/BP) heterostructures, demonstrating the first direct observation of in-plane anisotropic phonon polariton modes in vdW heterostructures. Notably, the measured in-plane optical anisotropy along the armchair and zigzag crystal axes exceeds the ratio of refractive indices of BP in the *x*-*y* plane. We explain that this enhancement is due to the high confinement of the phonon polaritons in h-BN. We observe a maximum in-plane optical anisotropy of $\alpha_{max} = 1.25$ in the frequency spectrum at 1405 to 1440 cm^{-1}. These results provide new insights into the behavior of polaritons in vdW heterostructures, and the observed anisotropy enhancement paves the way to novel nanophotonic devices and to a new way to characterize optical anisotropy in thin films.

INTRODUCTION

Phonon polaritons due to the coupling of photons and optical phonons in polar dielectrics such as hexagonal boron nitride (h-BN) have attracted much interest in the two-dimensional (2D) materials reseach field (*1*–*10*). Specifically, h-BN has light constituent elements, which lead to strong phonon resonances at mid-infrared (IR) frequencies (*10*). Such h-BN–based polaritonic systems exhibit confinement of light below the diffraction limit (*11*), propagation with ultralow losses (*3*), hyperbolic properties (*5*, *10*–*15*), and tunable response by changing the thickness of the samples (*10*) at mid-IR wavelengths. However, it is noteworthy that in the experiments performed so far, the substrates were optically isotropic. The effect of the substrate in-plane optical anisotropy ($\varepsilon_x \neq \varepsilon_y$, where ε_x and ε_y are the relative permittivities along the *x* and *y* axes) has not yet been investigated. It is therefore important to gain new insights into the interaction of polaritons with in-plane optically anisotropic substrates. In this work, we report a scattering-type scanning near-field optical microscopy (s-SNOM) (*16*, *17*) study of h-BN on black phosphorus (h-BN/BP) heterostructures, demonstrating the first direct observation of in-plane anisotropic phonon polariton waveguide modes supported by h-BN placed on BP, an in-plane anisotropic van der Waals (vdW) material (*18*–*20*). Remarkably, as explained later, the maximum anisotropy of the phonon polariton propagation along the *x* and *y* axes of our heterostructure exceeds the anisotropy of the vdW layers used to create it.

RESULTS

Our samples consist of a thin (40 nm) h-BN flake placed on BP on a SiO_2/Si substrate and then patterned into disc shapes (see figs. S1 to S3). Because of their rotational symmetry, any anisotropy in the polariton propagation would be clearly visible. In addition, and for the same reason, no careful alignment is needed between the patterns and the BP optical axes at the stage of device fabrication (see Supplementary Method 1). The phonon polaritons in h-BN and optical properties of BP have been explored in several works (*10*, *21*) and are briefly recalled here. h-BN (Fig. 1A) is a uniaxial anisotropic (or birefringent) material characterized by an in-plane relative dielectric permittivity, $\varepsilon_\perp$ (in the *x* and *y* directions of Fig. 1A), different from the out-of-plane one, $\varepsilon_\parallel$ (in the *z* direction). The polarization of the boron and nitrogen bond allows the coupling of optical phonons with incident mid-IR light, resulting in phonon polaritons. Because the unit cell contains two atoms, there are three optical phonon modes: two in-plane (degenerates because of the in-plane isotropy of h-BN) with a resonance at 1370 cm^{-1} and one out-of-plane with a lower resonance frequency at 780 cm^{-1}. The presence of the polaritons causes a negative permittivity in two different frequency bands, called reststrahlen bands, as shown in Fig. 1B [first reststrahlen band (RS1): 780 to 830 cm^{-1}; second reststrahlen band (RS2): 1370 to 1610 cm^{-1}] (*7*, *10*). In the RS1 band, the relative out-of-plane permittivity, $\varepsilon_\parallel$, is negative, whereas in the RS2 band, considered in this work, the relative in-plane permittivity, $\varepsilon_\perp$, is negative. As a result of these optical properties, h-BN supports highly confined guided transverse magnetic (TM) modes in these two bands (*7*, *10*). It is instructive to recall the propagation of TM plane waves (i.e., p-polarized) in h-BN. In this uniaxial material, the dispersion reads

$$\frac{k_\perp^2}{\varepsilon_{||}} + \frac{k_{||}^2}{\varepsilon_\perp} = k_0 = \frac{\omega^2}{c^2} \quad (1)$$

where $k_\perp$ and $k_\parallel$ are the in-plane and out-of-plane components of the wave vector, k_0 is the wave vector in vacuum at the frequency ω, and *c* is the speed of light. Equation 1 is represented graphically in Fig. 1C. The negative out-of-plane or in-plane permittivity in the reststrahlen bands enables the propagation of hyperbolic polaritons, which can have arbitrarily high wave vectors. This allows even thin flakes of h-BN to support an infinite number of guided modes theoretically (*10*). Unlike h-BN, BP is a non-polar dielectric and hence does not exhibit phonon polaritons. Whereas highly doped (or gated) BP supports plasmon polaritons (*22*), the undoped material used in this work does not (Table 1) and behaves as an anisotropic biaxial dielectric (with relative

[1]Harvard John A. Paulson School of Engineering and Applied Sciences, Harvard University, Cambridge, MA 02138, USA. [2]Department of Electrical Engineering, Howard University, Washington, DC 20059, USA. [3]Department of Physics, Harvard University, Cambridge, MA 02138, USA. [4]Center for Nanoscale Systems, Harvard University, Cambridge, MA 02138, USA.
*These authors contributed equally to this work.
†Corresponding author. Email: mtamagnone@seas.harvard.edu (M.T.); capasso@seas.harvard.edu (F.C.)

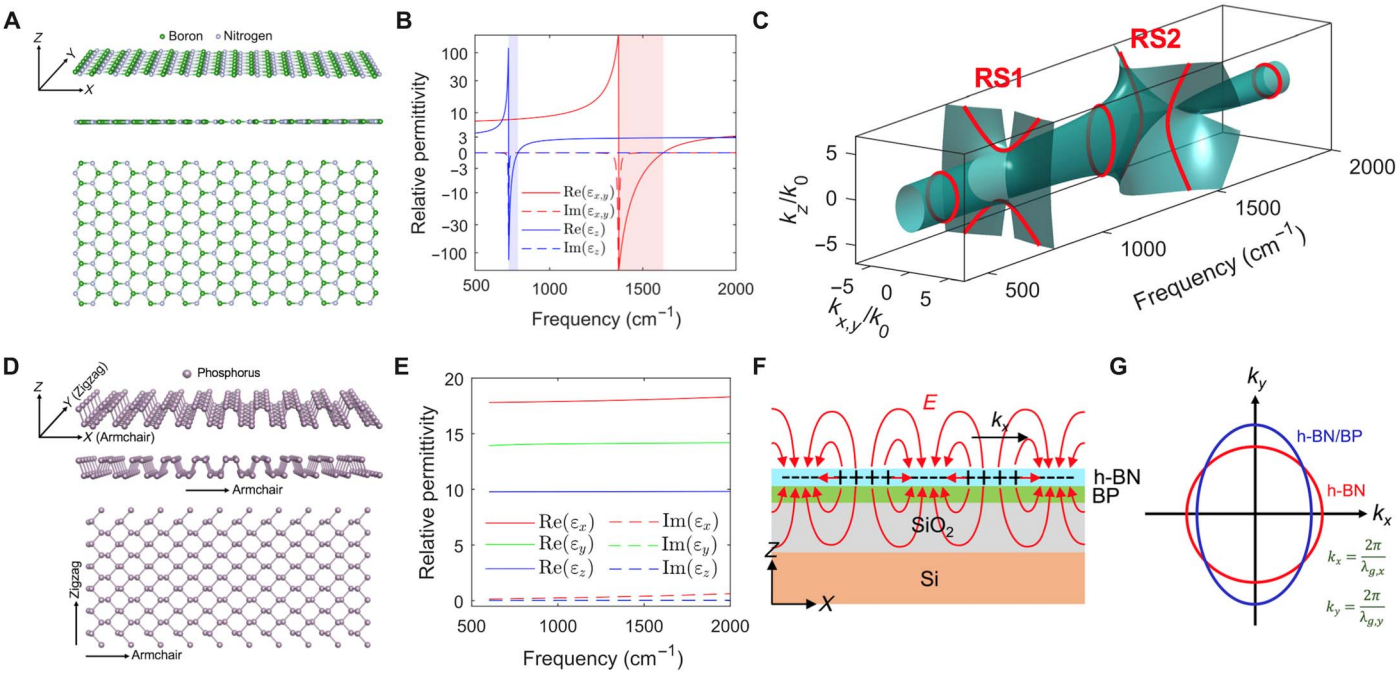

Fig. 1. Anisotropic phonon polariton propagation in the h-BN/BP heterostructure. (**A**) Schematic illustration of the crystal structure of h-BN. A single layer is shown. (**B**) Relative permittivities of h-BN along the different crystal axes showing hyperbolic behavior in two different frequency bands (highlighted in blue and red). (**C**) Schematic illustration of the hyperbolic dispersion relation of h-BN in the two different reststrahlen bands (RS1, 780 to 830 cm^{-1}; RS2, 1370 to 1610 cm^{-1}). (**D**) Schematic illustration of the puckered orthorhombic crystal structure of BP. A single layer is shown. In the in-plane anisotropic geometry of BP, the slow axis is along the armchair direction, whereas the zigzag direction represents the fast axis. (**E**) Relative permittivities of biaxial anisotropic BP along the different crystal axes (*21*). (**F**) Electric field profile of polaritons in the h-BN/BP heterostructure placed on a SiO_2/Si substrate. The electric field lines here are due to coupling of mid-IR photons to in-plane optical phonons in the RS2 band of h-BN. (**G**) The presence of an in-plane anisotropic substrate such as BP affects the propagation of phonon polariton along the armchair and zigzag crystal axes, resulting in approximately elliptical dispersion relation in the k_x-k_y plane in comparison to a circular dispersion relation for h-BN on SiO_2/Si. $\lambda_{g,x}$ and $\lambda_{g,y}$ are the guided wavelengths of phonon polariton modes along the *x* and *y* axes, respectively.

Table 1. Overview and spectral ranges in which different types of polaritons exist in h-BN, BP, and their heterostructure.

vdW material	Polariton type	Spectra range
h-BN	Phonon polaritons	780–830 cm^{-1}, 1370–1610 cm^{-1}
Undoped BP	(No polaritons)	–
Doped/gated BP	Anisotropic plasmon polaritons	~200–4000 cm^{-1}
h-BN/BP heterostructure	Anisotropic phonon polaritons	780–830 cm^{-1}, 1370–1610 cm^{-1}

permittivities, $\varepsilon_x \neq \varepsilon_y \neq \varepsilon_z$, and $n_{x,y,z} = \sqrt{\varepsilon_{x,y,z}}$). The puckered orthorhombic geometry of BP (*18*–*20*) results in the in-plane optical anisotropy, with the crystal axes (armchair and zigzag) exhibiting different refractive indices (Fig. 1, D and E). The in-plane optical anisotropy is prominent in the entire optical spectrum of interest from ultraviolet to IR (*21*–*23*), which allows the determination of the crystal axes using angle-resolved polarized Raman (ARPR) spectroscopy (fig. S1, A and B) (*24*). The same task can be achieved with polarized light microscopy (fig. S2). Figure 1F illustrates the electric field lines of the excited fundamental guided phonon polariton mode supported by h-BN. Here, the field lines are influenced by the presence of BP and its in-plane anisotropy, which causes the in-plane guided polariton modes to be in-plane anisotropic as well. More precisely, for a constant illumination wavelength, the polaritons will propagate with different effective indices along the different in-plane crystal axes of BP. Figure 1G qualitatively compares contour plot of dispersion relation at a given frequency of isotropic phonon polariton modes in h-BN to that of anisotropic phonon polariton modes in the h-BN/BP heterostructure. The dispersion relation of anisotropic phonon polaritons in the h-BN/BP heterostructure is approximated by an ellipse in the k_x-k_y plane as opposed to a circle for the case of isotropic phonon polaritons in h-BN (*14*). We then define the polariton anisotropy α as

$$\alpha = \frac{n_{\mathrm{eff},x}}{n_{\mathrm{eff},y}} \tag{2}$$

where $n_{\mathrm{eff},x}$ and $n_{\mathrm{eff},y}$ are the effective indices of the guided polariton modes in the *x* (armchair) and *y* (zigzag) directions, respectively. Notably, the polariton anisotropy, α, defined with the effective indices of the modes in the h-BN/BP heterostructure, can be larger than the ratio (α′) of the refractive indices of BP in the *x*-*y* plane

$$\alpha' = \frac{n_x}{n_y} \tag{3}$$

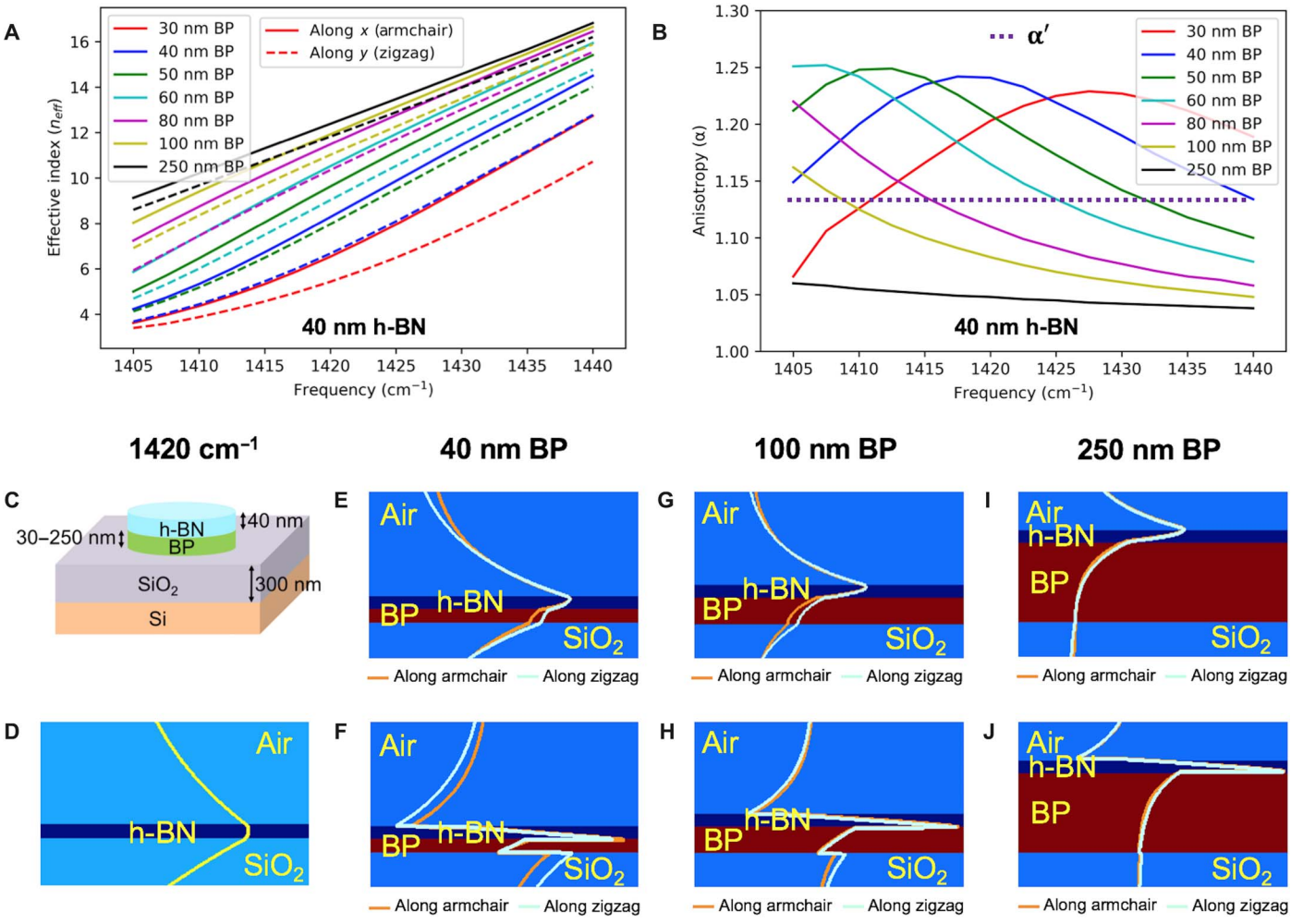

Fig. 2. Calculation of anisotropic dispersion relation of the h-BN/BP heterostructure. (**A**) For a given thickness (40 nm) of h-BN, the effective indices of phonon polariton modes along both the armchair and zigzag crystal axes of BP increase monotonically with thickness of BP and frequencies in the range of 1405 to 1440 cm^{-1} due to the increased mode confinement factor. (**B**) Calculated anisotropy values of the phonon polaritons for varying thickness of BP. For each frequency, there is an optimum thickness of BP that results in maximum anisotropy. Similarly, for each thickness of BP, there is an optimum frequency at which the anisotropy is maximum. The dashed purple line represents the ratio of refractive indices of BP in the *x*-*y* plane. The calculated in-plane anisotropy of the h-BN/BP heterostructure is larger ($\alpha_{max} = 1.25$) than the ratio of refractive indices of BP in the *x*-*y* plane ($\alpha' = 1.13$). (**C**) Schematic of the h-BN/BP heterostructure used to calculate the effective indices in (A) and anisotropy in (B). For a fixed 40-nm-thick h-BN, the thickness of BP is varied between 30 and 250 nm. (**D** to **J**) Electric field profiles at 1420 cm^{-1}. (D) Electric field profile with no BP. The mode is TM, and only the field component parallel to the propagation direction is plotted. Electric field is confined in h-BN, demonstrating a guided polariton mode. The electric field intensity decays away from h-BN surfaces in air and SiO$_2$. (E and F) Electric field profile with 40-nm BP, representing calculated in-plane and out-of-plane field components, respectively. The electric field confinement along the *x* axis (armchair) is larger than that along the *y* axis (zigzag), implying anisotropic effective indices along the *x* and *y* crystal axes of BP. (G and H) Electric field profile with 100-nm BP representing in-plane and out-of-plane field components, respectively. The electric field confinement along both the *x* and *y* axes is comparable, implying lower anisotropy in comparison to the case with 40-nm BP. Higher confinement with 100-nm BP also demonstrates larger effective indices compared to the case with 40-nm BP. (I and J) Electric field profile with 250-nm BP representing in-plane and out-of-plane field components, respectively. Like the case with 100-nm BP, the electric field confinement along both the *x* and *y* axes is comparable, implying lower anisotropy in comparison to the case with 40-nm BP. Higher confinement in (I) and (J) also demonstrates larger effective indices compared to the case with 40- and 100-nm BP.

The guided modes in this heterostructure therefore exhibit an enhanced anisotropy with respect to BP alone. Figure 2A shows the effect of thickness of BP on the calculated (using Lumerical MODE Solutions) effective indices of the phonon polariton modes along the armchair and zigzag axes of BP. In the frequency spectrum at 1405 to 1440 cm^{-1}, there is a clear evidence of anisotropy in the phonon polariton propagation along the armchair and zigzag axes given by the difference in their effective indices. The effective indices along both the armchair and zigzag directions increase with frequency.

Figure 2B demonstrates the in-plane anisotropy, α, of phonon polariton propagation in h-BN/BP heterostructures (Fig. 2C). The dashed purple line represents the ratio of refractive indices of BP in the *x*-*y* plane, α′. As mentioned earlier, there are wide spectral ranges where α exceeds α′. This effect can be understood as follows: Let us consider a polariton propagating along the zigzag direction for a BP thickness such that polariton fields are partially inside BP. When propagation along the armchair axis is considered, the electric field (which is partially polarized along the wave vector) interacts with a higher permittivity,

which slows down the wave propagation. However, this also implies that the field is now more confined, i.e., a larger fraction of it is inside h-BN. This additional effect further reduces the phase velocity, enhancing the anisotropy. Additional insights are shown in fig. S9, which studies the dependence of the effective index n_{eff} of the polariton with respect to the in-plane refractive index n of BP. In reality, n can only take the two values corresponding to the two axes of BP, but this theoretical study highlights the fact that the function $n_{eff}(n)$ is not linear and has a sigmoidal shape instead due to the aforementioned argument on confinement. At the inflection point of the sigmoid, the slope is maximum, which means that a variation in n will cause a greater variation in n_{eff}. This behavior explains the enhancement observed in the anisotropy, which peaks for those frequencies and thicknesses for which the inflection point is located between $n = 4.24$ and $n = 3.74$ (the refractive indices of BP along the x and y crystal axes). The inflection point (and hence the maximum of the anisotropy) occurs when the evanescent field tail of the polaritons is comparable to the thickness of BP. Therefore, for larger BP thickness, the maximum anisotropy occurs at lower frequency, where the evanescent tail extends farther away from h-BN. This argument perfectly explains the observed trend of the anisotropy maxima. As shown in Fig. 2B, for each frequency, there is an optimum thickness of BP, which maximizes the in-plane anisotropy. Similarly, for each thickness of BP, there is an optimum frequency that maximizes the in-plane optical anisotropy. In the large frequency limit (i.e., 1440 cm^{-1}), the in-plane optical anisotropy decreases with increasing thickness of BP. Similarly, for a given thickness of BP (i.e., 40 nm), on varying the thickness of h-BN in the range of 10 to 40 nm, we observe a larger in-plane anisotropy of the polaritons (with a maximum anisotropy of ~1.3).

Figure 2D shows the electric field profile of h-BN on a SiO_2/Si substrate, where the electric field is mostly confined in h-BN and exponentially decays away from the h-BN surfaces in air and SiO_2. The confinement of polariton mode in h-BN along the x-y plane increases with increasing BP thickness (Fig. 2, E, G, and I), which allows weaker interaction with the in-plane anisotropic refractive indices of BP. For 40-nm BP, the polariton mode is less confined in h-BN, which allows a stronger interaction with BP and leads to a higher difference in phonon polariton propagation along the armchair and zigzag crystal axes. Similarly, the dispersion behavior of anisotropy can be explained by the fact that mode confinement in h-BN, for a given thickness of BP, is a function of frequency, where the modes are highly confined for larger frequencies (Fig. 2A). Similarly, Fig. 2 (F, H, and J) demonstrates the electric field profile along the out-of-plane axis of the h-BN/BP heterostructure.

To probe the fundamental guided mode of the anisotropic phonon polaritons in the h-BN/BP heterostructure, we used s-SNOM, which allows imaging of guided modes in the mid-IR spectrum. We used a quantum cascade laser (QCL) as a source focused by a parabolic mirror to a region of sample and to the probe [a PtIr-coated atomic force microscopy (AFM) tip]. Scattering of the laser beam at the tip (diameter, ~20 nm) provides wave vector matching and excites/probes the phonon polariton modes in h-BN (Fig. 3, A to C) in the RS2 band of h-BN. An interferometer and a pseudo-heterodyne detection scheme are used to extract the amplitude and phase of the phonon polaritons in the h-BN/BP heterostructure (*16*). The s-SNOM produces images that include both the amplitude and the phase of the scattered field at each pixel of the scan (raw scans are reported in fig. S4), which can be obtained by using several harmonics of the pseudo-heterodyne detection. As explained in our previous works (*6*, *25*), the complex-valued images are not a simple representation of the near fields of the structure, but rather are a superposition of several contributions. Each contribution is associated to a particular path that the light follows when interacting with the tip-sample system, and all the contributions are added together in the final detected image. The contributions and the final image are represented by complex-valued images. For samples supporting no guided waves or standing resonances, only one path is relevant, which we call material contribution, and it is associated with the light path from the interferometer to the tip, which enhances light intensity on the material directly underneath it and then scatters it back to the interferometer (Fig. 3A). This contribution is affected by the local material polarizability directly below the AFM tip.

When guided waves are supported, other contributions are possible. However, no guided wave can be detected unless there is an edge or any other scatterer on the sample. In our case, the samples are discs, the edge of which allows the detection of guided waves. Two possible paths contribute to the detection of the guided modes in the sample, and they are associated to the roundtrip and direct contributions. In the roundtrip contribution, the tip couples the QCL light into the guided mode, which is reflected by the edge of the sample and is then scattered back to the detector by the tip (Fig. 3B). In the direct contribution, the light from the QCL is scattered by the edge into the guided mode, and then the tip scatters it back to the detector (Fig. 3C). Hence, from the raw images (fig. S4), we first remove the material contribution and then we separate the direct and roundtrip components exploiting the rotational symmetry of the system, as explained in Supplementary Method 1 and fig. S5.

The roundtrip contribution is unaffected by possible misalignments (see Supplementary Method 1) of the laser beam with respect to the crystal axes of BP, and hence, it is used for further analysis of the in-plane anisotropy of the polaritons in h-BN/BP heterostructures (Fig. 3, E to L). For a reference sample without BP (fig. S5A), circular fringes are observed as expected from previous experiments (*14*). The presence of BP affects the phonon polaritons in h-BN and results in an anisotropic propagation given by the elliptical fringes with increased ellipticity toward the center of the disc. The orientation of the major and minor axes of ellipses represents the crystal axes of BP and matches that of the crystal axes measured using ARPR spectroscopy (fig. S1, A and B). Figure 3 (E to H) shows the frequency dependence of the roundtrip contribution of the phonon polaritons in the 40-nm h-BN/40-nm BP heterostructure, whereas Fig. 3 (I to L) shows the frequency dependence of phonon polaritons in the 40-nm h-BN/250-nm BP heterostructure. Elliptical fringes are observed for both the 40-nm and 250-nm BP heterostructures, and the effective indices can be extracted from the fringe spacing measured, as illustrated in Fig. 3D. More precisely, the spacing between fringes is half of the guided wavelength of the mode because the waves propagate back and forth along the distance from the tip to the edge. The increased ellipticity of the fringes toward the center can be represented by the following expressions: $a = \frac{m\lambda_{g,x}}{2}$ and $= \frac{m\lambda_{g,y}}{2}$, where a and b are the distances from the first fringe ($m = 0$) to the mth fringe along the x and y crystal axes, respectively; m is a positive integer; and $\lambda_{g,x}$ and $\lambda_{g,y}$ are the guided polariton wavelengths along the x and y crystal axes, respectively. The effective index increases with increasing frequency (Fig. 3M) as expected for phonon polaritons in h-BN. There is a good agreement between the calculated effective indices and the measured effective indices using s-SNOM near-field images despite the fact that no fit was used. Instead, we use a theoretical prediction, starting from the measured thickness of the sample and from calculated values of the refractive indices of BP in (*21*).

Thicker BP (in the semi-infinite limit) allows a larger effective index, but the in-plane anisotropy is weaker. Hence, the heterostructure results

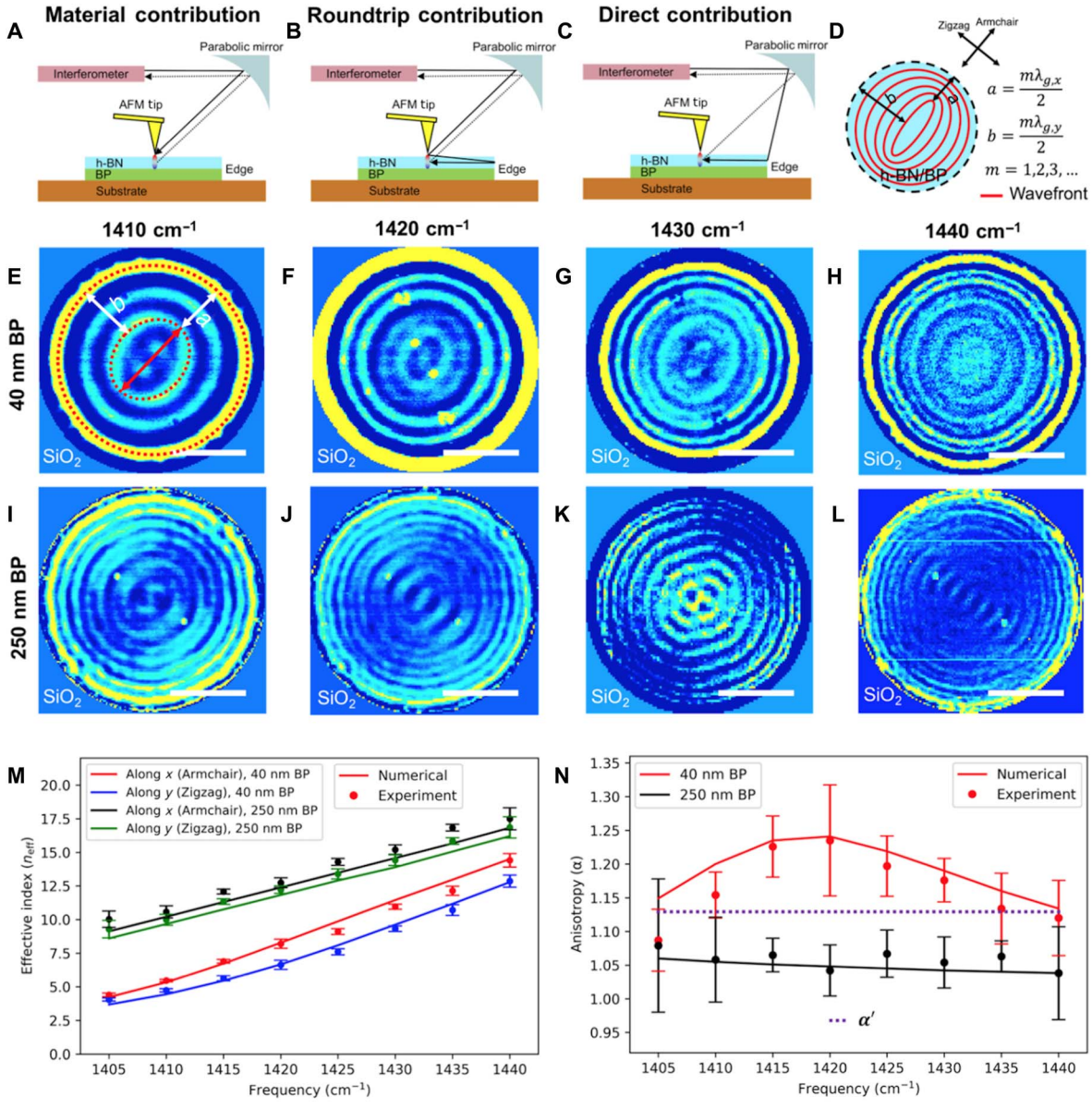

Fig. 3. Anisotropic dispersion relation of h-BN/BP heterostructure discs. (**A**) Schematic illustration of material contribution. The incident IR beam goes to the tip, which focuses light on the material directly underneath and then scatters it back to the interferometer. (**B**) Schematic illustration of the roundtrip contribution. The incident IR beam scatters off the AFM tip, gets reflected from the edge of the h-BN/BP heterostructure, and gets scattered again off the AFM tip to the interferometer, resulting in a round trip of the phonon polariton mode. (**C**) Schematic illustration of direct contribution. In this case, the incident IR beam gets coupled to the phonon polariton mode at the edge of the h-BN/BP heterostructure and scatters off the AFM tip to the interferometer. (**D**) Mathematical representation of the elliptical fringes of the roundtrip contribution in the presence of BP. *a* and *b* represent the distance from $m = 0$ fringe to *m*th fringe along the major and minor axes of the *m*th ellipse, respectively. Anisotropy (α) is given by $\alpha = \frac{b}{a}$. Ellipticity of the fringe increases with *m*. (**E** to **H**) Real parts of the roundtrip contribution of the s-SNOM image in fig. S3B for the 40-nm h-BN/40-nm BP heterostructure at varying frequencies. Dashed red circle in (E) represents the 0th ($m = 0$) fringe, and the dashed red ellipse represents the 2nd ($m = 2$) fringe. *a* and *b* are the distances from the 0th fringe to the major and minor axes of the 2nd fringe, respectively. Arrow represents the direction of the electric field of the illuminating beam. (**I** to **L**) Real parts of the roundtrip contribution of s-SNOM image in fig. S3D for the 40-nm h-BN/250-nm BP heterostructure at varying frequencies. The number of fringes in the h-BN/BP disc increases with frequency, implying increased confinement of the phonon polaritons in the h-BN/BP heterostructure. At a given frequency, the mode confinement is larger for thicker BP. (**M**) Effective indices in both the 40-nm h-BN/40-nm BP and 40-nm h-BN/250-nm BP heterostructures increase with increasing frequencies, implying higher mode confinement as evident in (E) to (L). Mode confinement is higher for thicker BP, which demonstrates the substrate's thickness-dependent confinement. On the other hand, the effective indices along the armchair axis are larger than those along the zigzag axis for both the heterostructures. The effective index contrast is lower for the 40-nm h-BN/250-nm BP heterostructure, implying a lower anisotropy in comparison to the 40-nm h-BN/40-nm BP heterostructure. There is an excellent agreement between theory and experiments without the need of fitting any of the parameters of the structure. (**N**) Anisotropy $\left(\alpha = \frac{b}{a}\right)$ of the phonon polaritons at varying frequencies. In the frequency range of 1405 to 1440 cm^{-1}, the anisotropy monotonically decreases for the 40-nm h-BN/250-nm BP heterostructure. The anisotropy is lower in comparison to the ratio of refractive indices of BP in the *x*-*y* plane shown by dashed-purple line. Notably, the anisotropy of the 40-nm h-BN/40-nm BP heterostructure peaks at 1420 cm^{-1} with a maximum value of $\alpha_{max} = 1.25$. The anisotropy values are much higher in comparison to the ratio of refractive indices of BP in the *x*-*y* plane, i.e., $\alpha_{max} > \alpha'$. Thus, the phonon polaritons in h-BN act as a means of enhancing the in-plane optical anisotropy of h-BN/BP heterostructures. Scale bars, 2 μm.

in fringes with lower ellipticity away from the sample center. For 40-nm BP, the in-plane anisotropy peaks at 1420 cm^{-1} (Fig. 3N). On the other hand, the anisotropy decreases monotonically with frequency for 250-nm BP. There is an excellent agreement between the calculated and experimental in-plane anisotropy. The maximum possible anisotropy given by the ratio of refractive indices of BP in the *x*-*y* plane (*21*) is $\alpha' = 1.13$, but the calculated and experimental values show a much higher maximum anisotropy of $\alpha_{max} = 1.25$ for 40-nm BP at 1420 cm^{-1}. This confirms the in-plane anisotropy enhancement (and for the first time) in the h-BN/BP heterostructure described above. Similarly, in-plane anisotropy can be probed in the RS1 of h-BN, but QCLs for this range are not available (*6*). We verified that rotating the sample by 90° causes a rotation of the fringe orientation, as expected for an anisotropic sample (fig. S5). Similar results are observed for all the harmonics of the pseudo-heterodyne detection used in our s-SNOM system (fig. S6).

DISCUSSION

We expect that the ability of engineering these deeply subwavelength modes will have important applications in mid-IR nanophotonics from probing the in-plane optical anisotropy of other vdW materials and heterostructures in mid-IR, which is clearly not available, to new approaches for designing vertically stacked heterostructures with extreme light confinement and tailored optical properties. For example, the heterostructure consisting of BP/h-BN/BP can lead to an even higher in-plane optical anisotropy, up to $\alpha = 1.5$ (fig. S7). Furthermore, our study can be extended to other heterostructures that are electrostatically gated to tune in-plane optically anisotropic substrates, such as BP and ReS_2 (*26*), to result in tunable phonon polaritons supported by polar dielectric materials, such as h-BN and SiC (*16*, *17*), and tunable plasmon polaritons supported by graphene (*27*, *28*).

MATERIALS AND METHODS

Sample fabrication

BP flakes were mechanically exfoliated onto a 300-nm SiO_2/Si substrate in the Ar glovebox, which has less than 0.1 ppm (parts per million) of O_2 and H_2O to preserve the flakes from deterioration. h-BN flakes were similarly exfoliated on the substrate. The thickness of flakes was confirmed with AFM (Park AFM). We used a dry transfer technique with polymer (polycarbonate) and polydimethylsiloxane stamp to fabricate h-BN/BP heterostructures in the Ar glovebox. Substrates were then coated with poly(methyl methacrylate) (PMMA) 950(A6) and exposed with an electron beam system with a dose of 450 $\mu C/cm^2$ using an accelerating voltage of 30 kV. After developing in methyl isobutyl ketone for 1 min, reactive ion etching using a mixture of CHF_3, Ar, and O_2 at flows of 10, 5, and 2 sccm, respectively, and a radio frequency generator at 30 W for 3 to 6 min was subsequently used to shape the heterostructure into discs. After the etching process, PMMA was removed by acetone, rinsed with isopropyl alcohol, and dried with nitrogen.

ARPR spectroscopy

ARPR spectroscopy was performed using a 532-nm laser in a Horiba system. The power incident on BP was kept below 2.5 mW to avoid sample damage. Parallel polarization was used to collect the Raman signals. BP samples were rotated 360° about the microscope optical axis in 36 steps (10° per step). The grating number of the detector was set to 1800, and the spectral range was from 300 to 500 cm^{-1}. The acquisition time was set to 10 s for three times accumulation to minimize the laser damage.

Numerical simulations

1D solver (Lumerical MODE Solutions) with a mesh size of 1 nm was used to compute the fundamental mode profile and effective indices of h-BN/BP vdW heterostructures for a range of frequencies in the RS2 band of h-BN. We calculated the effective indices for a range (30 to 250 nm) of thickness of BP with a given thickness of h-BN (40 nm). Here, h-BN was modeled as an anisotropic dielectric, with its permittivity values obtained from the Lorentz model (*6*, *10*, *25*). Besides, BP was modeled as an anisotropic dielectric, with its permittivity values obtained from Valagiannopoulos *et al.* (*21*).

Scattering-type scanning near-field optical microscopy

The near-field scans were obtained using a commercially available s-SNOM from NeaSpec, which is based on a tapping-mode AFM. QCL was used as a tunable mid-IR source from Daylight Solutions. An IR beam from a QCL was focused onto a PtIr-coated Si tip (diameter, ~20 nm) to launch the phonon polariton modes. The backscattered signal was demodulated at the higher pseudo-heterodyne harmonics ($n \geq 2$) to reduce the background. Details of the separation of the direct, roundtrip, and material contrast contributions are presented in the Supplementary Materials.

SUPPLEMENTARY MATERIALS

Supplementary material for this article is available at http://advances.sciencemag.org/cgi/content/full/5/4/eaau7171/DC1

Supplementary Method 1. Separation of s-SNOM contributions

Supplementary Method 2. Effective index, electric field profile, and anisotropy calculations

Fig. S1. Optical and Raman characterization.

Fig. S2. Microscope imaging using polarized light.

Fig. S3. AFM characterization.

Fig. S4. Raw s-SNOM scans.

Fig. S5. Component separation.

Fig. S6. s-SNOM images of the real part of the roundtrip contribution at different pseudo-heterodyne harmonics.

Fig. S7. Three-layer heterostructures.

Fig. S8. Calculated in-plane anisotropy values of the phonon polaritons for varying thickness of h-BN in the h-BN/BP heterostructure.

Fig. S9. Calculated effective indices for a range of refractive indices of BP.

REFERENCES AND NOTES

1. D. N. Basov, M. M. Fogler, F. J. García de Abajo, Polaritons in van der Waals materials. *Science* **354**, aag1992 (2016).
2. T. Low, A. Chaves, J. D. Caldwell, A. Kumar, N. X. Fang, P. Avouris, T. F. Heinz, F. Guinea, L. Martin-Moreno, F. Koppens, Polaritons in layered two-dimensional materials. *Nat. Mater.* **16**, 182–194 (2017).
3. A. J. Giles, S. Dai, I. Vurgaftman, T. Hoffman, S. Liu, L. Lindsay, C. T. Ellis, N. Assefa, I. Chatzakis, T. L. Reinecke, J. G. Tischler, M. M. Fogler, J. H. Edgar, D. N. Basov, J. D. Caldwell, Ultralow-loss polaritons in isotopically pure boron nitride. *Nat. Mater.* **17**, 134–139 (2018).
4. Z. Shi, H. A. Bechtel, S. Berweger, Y. Sun, B. Zeng, C. Jin, H. Chang, M. C. Martin, M. B. Raschke, F. Wang, Amplitude- and phase-resolved nanospectral imaging of phonon polaritons in hexagonal boron nitride. *ACS Photonics* **2**, 790–796 (2015).
5. P. Li, F. J. Alfaro-Mozaz, F. Casanova, L. E. Hueso, S. Liu, J. H. Edgar, A. Y. Nikitin, S. Vélez, R. Hillenbrand, Infrared hyperbolic metasurface based on nanostructured van der Waals materials. *Science* **359**, 892–896 (2018).
6. A. Ambrosio, M. Tamagnone, K. Chaudhary, L. A. Jauregui, P. Kim, W. L. Wilson, F. Capasso, Selective excitation and imaging of ultraslow phonon polaritons in thin hexagonal boron nitride crystals. *Light Sci. Appl.* **7**, 27 (2018).
7. J. D. Caldwell, L. Lindsay, V. Giannini, I. Vurgaftman, T. L. Reinecke, S. A. Maier, O. J. Glembocki, Low-loss, infrared and terahertz nanophotonics using surface phonon polaritons. *Nanophotonics* **4**, 44–68 (2015).

8. E. Yoxall, M. Schnell, A. Y. Nikitin, O. Txoperena, A. Woessner, M. B. Lundeberg, F. Casanova, L. E. Hueso, F. H. L. Koppens, R. Hillenbrand, Direct observation of ultraslow hyperbolic polariton propagation with negative phase velocity. *Nat. Photon.* **9**, 674–678 (2015).
9. K. L. Tsakmakidis, Ultraslow waves on the nanoscale. *Science* **358**, eaan5196 (2017).
10. S. Dai, Z. Fei, Q. Ma, A. S. Rodin, M. Wagner, A. S. McLeod, M. K. Liu, W. Gannett, W. Regan, K. Watanabe, T. Taniguchi, M. Thiemens, G. Dominguez, A. H. Castro Neto, A. Zettl, F. Keilmann, P. Jarillo-Herrero, M. M. Fogler, D. N. Basov, Tunable phonon polaritons in atomically thin van der Waals crystals of boron nitride. *Science* **343**, 1125–1129 (2014).
11. J. D. Caldwell, A. V. Kretinin, Y. Chen, V. Giannini, M. M. Fogler, Y. Francescato, C. T. Ellis, J. G. Tischler, C. R. Woods, A. J. Giles, M. Hong, K. Watanabe, T. Taniguchi, S. A. Maier, K. S. Novoselov, Sub-diffractional volume-confined polaritons in the natural hyperbolic material hexagonal boron nitride. *Nat. Commun.* **5**, 5221 (2014).
12. P. Li, M. Lewin, A. V. Kretinin, J. D. Caldwell, K. S. Novoselov, T. Taniguchi, K. Watanabe, F. Gaussmann, T. Taubner, Hyperbolic phonon-polaritons in boron nitride for near-field optical imaging and focusing. *Nat. Commun.* **6**, 1–9 (2015).
13. A. Kumar, T. Low, K. H. Fung, P. Avouris, N. X. Fang, Tunable light–matter interaction and the role of hyperbolicity in graphene–hBN system. *Nano Lett.* **15**, 3172–3180 (2015).
14. A. Ambrosio, L. A. Jauregui, S. Dai, K. Chaudhary, M. Tamagnone, M. M. Fogler, D. N. Basov, F. Capasso, P. Kim, W. L. Wilson, Mechanical detection and imaging of hyperbolic phonon polaritons in hexagonal boron nitride. *ACS Nano* **11**, 8741–8746 (2017).
15. J. Duan, R. Chen, J. Li, K. Jin, Z. Sun, J. Chen, Launching phonon polaritons by natural boron nitride wrinkles with modifiable dispersion by dielectric environments. *Adv. Mater.* **29**, 1–8 (2017).
16. A. Huber, N. Ocelic, D. Kazantsev, R. Hillenbranda, Near-field imaging of mid-infrared surface phonon polariton propagation. *Appl. Phys. Lett.* **87**, 081103 (2005).
17. A. J. Huber, N. Ocelic, R. Hillenbrand, Local excitation and interference of surface phonon polaritons studied by near-field infrared microscopy. *J. Microsc.* **229**, 389–395 (2008).
18. X. Ling, H. Wang, S. Huang, F. Xia, M. S. Dresselhaus, The renaissance of black phosphorus. *Proc. Natl. Acad. Sci. U.S.A.* **112**, 4523–4530 (2015).
19. F. Xia, H. Wang, Y. Jia, Rediscovering black phosphorus as an anisotropic layered material for optoelectronics and electronics. *Nat. Commun.* **5**, 1–6 (2014).
20. F. Xia, H. Wang, D. Xiao, M. Dubey, A. Ramasubramaniam, Two-dimensional material nanophotonics. *Nat. Photonics* **8**, 899–907 (2014).
21. C. A. Valagiannopoulos, M. Mattheakis, S. N. Shirodkar, E. Kaxiras, Manipulating polarized light with a planar slab of black phosphorus. *J. Phys. Commun.* **1**, 045003 (2017).
22. T. Low, Plasmons and screening in monolayer and multilayer black phosphorus. *Phys. Rev. Lett.* **113**, 106802 (2014).
23. H. Asahina, A. Morita, Band structure and optical properties of black phosphorus. *J. Phys. C Solid State Phys.* **17**, 1839–1852 (1984).
24. J. Wu, N. Mao, L. Xie, H. Xu, J. Zhang, Identifying the crystalline orientation of black phosphorus using angle-resolved polarized Raman spectroscopy. *Angew. Chem. Int. Ed.* **54**, 2366–2369 (2015).
25. M. Tamagnone, A. Ambrosio, K. Chaudhary, L. A. Jauregui, P. Kim, W. L. Wilson, F. Capasso, Ultra-confined mid-infrared resonant phonon polaritons in van der Waals nanostructures. *Sci. Adv.* **4**, eaat7189 (2018).
26. D. A. Chenet, O. B. Aslan, P. Y. Huang, C. Fan, A. M. van der Zande, T. F. Heinz, J. C. Hone, In-plane Anisotropy in Mono- and Few-Layer ReS_2 probed by Raman spectroscopy and scanning transmission electron microscopy. *Nano Lett.* **15**, 5667–5672 (2015).
27. Z. Fei, A. S. Rodin, G. O. Andreev, W. Bao, A. S. McLeod, M. Wagner, L. M. Zhang, Z. Zhao, M. Thiemens, G. Dominguez, M. M. Fogler, A. H. Castro Neto, C. N. Lau, F. Keilmann, D. N. Basov, Gate-tuning of graphene plasmons revealed by infrared nano-imaging. *Nature* **487**, 82–85 (2012).
28. J. Chen, M. Badioli, P. Alonso-González, S. Thongrattanasiri, F. Huth, J. Osmond, M. Spasenović, A. Centeno, A. Pesquera, P. Godignon, A. Z. Elorza, N. Camara, F. J. García de Abajo, R. Hillenbrand, F. H. Koppens, Optical nano-imaging of gate-tunable graphene plasmons. *Nature* **487**, 77–81 (2012).

Acknowledgments: We thank M. Mattheakis for the discussions. **Funding:** This work was supported by NSF EFRI award no. 1542807. This work was performed, in part, at the Center for Nanoscale Systems (CNS), a member of the National Nanotechnology Coordinated Infrastructure Network (NNCI), which is supported by the NSF under NSF award no. 1541959. M.T. acknowledges the support of the Swiss National Science Foundation (SNSF) (grant nos. 168545 and 177836). M.R. and D.K.B. acknowledge the support of the Science and Technology Center for Integrated Quantum Materials, NSF (grant no. DMR-1231319). **Author contributions:** K.C., M.T., and F.C. devised experiments. M.R. and D.K.B. fabricated the samples. K.C., M.T., and A.A. performed s-SNOM scans. K.C. and M.T. analyzed the experimental data. K.C., M.T., P.K., and F.C. prepared the manuscript with input from all authors. All authors contributed to discussions and manuscript revision. **Competing interests:** The authors declare that they have no competing interests. **Data and materials availability:** All data needed to evaluate the conclusions in the paper are present in the paper and/or the Supplementary Materials. Additional data related to this paper may be requested from the authors.

Submitted 9 July 2018
Accepted 14 February 2019
Published 12 April 2019
10.1126/sciadv.aau7171

Citation: K. Chaudhary, M. Tamagnone, M. Rezaee, D. K. Bediako, A. Ambrosio, P. Kim, F. Capasso, Engineering phonon polaritons in van der Waals heterostructures to enhance in-plane optical anisotropy. *Sci. Adv.* **5**, eaau7171 (2019).

Science Advances

Engineering phonon polaritons in van der Waals heterostructures to enhance in-plane optical anisotropy

Kundan Chaudhary, Michele Tamagnone, Mehdi Rezaee, D. Kwabena Bediako, Antonio Ambrosio, Philip Kim and Federico Capasso

Sci Adv **5** (4), eaau7171.
DOI: 10.1126/sciadv.aau7171